Global correlations between winds and ocean chlorophyll

M. Kahru,[1] S. T. Gille,[1] R. Murtugudde,[2] P. G. Strutton,[3] M. Manzano-Sarabia,[4] H. Wang,[1] and B. G. Mitchell[1]

Received 2 July 2010; revised 23 August 2010; accepted 1 October 2010; published 16 December 2010.

[1] Global time series of satellite-derived winds and surface chlorophyll concentration (*Chl-a*) show patterns of coherent areas with either positive or negative correlations. The correlation between *Chl-a* and wind speed is generally negative in areas with deep mixed layers and positive in areas with shallow mixed layers. These patterns are interpreted in terms of the main limiting factors that control phytoplankton growth, i.e., either nutrients that control phytoplankton biomass in areas with positive correlation between *Chl-a* and wind speed or light that controls phytoplankton biomass in areas with negative correlation between *Chl-a* and wind speed. More complex patterns are observed in the equatorial regions due to regional specificities in physical-biological interactions. These correlation patterns can be used to map out the biogeochemical provinces of the world ocean in an objective way.

Citation: Kahru, M., S. T. Gille, R. Murtugudde, P. G. Strutton, M. Manzano-Sarabia, H. Wang, and B. G. Mitchell (2010), Global correlations between winds and ocean chlorophyll, *J. Geophys. Res.*, *115*, C12040, doi:10.1029/2010JC006500.

1. Introduction

[2] Phytoplankton productivity and biomass in the world ocean are limited by nutrient (N, P, Si, Fe) concentrations [*Chisholm and Morel*, 1991] and/or the mean light level, which is modulated by vertical mixing and seasonal variability in daily insolation [*Siegel et al.*, 2002]. Phytoplankton productivity drives the oceanic biological pump and therefore has the potential to affect global atmospheric CO_2 levels [*Sarmiento and Orr*, 1991]. Changes in atmospheric CO_2 and the associated climate forcing can in turn impact phytoplankton productivity by changing ocean stratification, circulation, and pH. A number of authors [*Platt and Sathyendranath*, 1988; *Longhurst et al.*, 1995] have proposed the definition and use of quasi-stable biogeochemical provinces as a means of assessing basin scale oceanic productivity and biogeochemical characteristics. These provinces were traditionally based on measurements from ship-based platforms with the obvious consequence that the observed properties were dramatically undersampled in both space and time and the resulting boundaries were not well defined. Global time series of satellite measurements provide a significant amount of data to classify ocean environments as different biogeochemical provinces and to monitor the interannual and long-term changes in province boundaries. A number of different methods have been proposed to differentiate between biogeochemical provinces. These include the annual variability in phytoplankton pigment concentration [*Esaias et al.*, 2000]; remotely sensed chlorophyll concentration, sea surface temperature, and the fixed boundaries of Longhurst's provinces [*Devred et al.*, 2007]; a bioinformatic clustering algorithm using water-leaving radiance at two wavelengths and the sea surface temperature [*Oliver and Irwin*, 2008]; and a fuzzy logic classification of ocean bio-optical signatures [*Moore et al.*, 2009]. Ocean ecosystems are governed by physical forcing, including winds, and studies of the relationships between winds and ocean biology have a long history [e.g., *Denman*, 1973]. However, global, high-resolution data sets of winds and phytoplankton data have not been available until recently. Here we use the correlation between time series of satellite-derived winds and surface chlorophyll-*a* concentration (*Chl-a*, mg m^{-3}) to map the main biogeochemical provinces in the world ocean based on the dominant mechanisms responsible for the variability in phytoplankton biomass.

2. Data and Methods

[3] Chlorophyll-*a* concentrations (*Chl-a*, mg m^{-3}) were obtained from NASA's Ocean Color Web site [*McClain*, 2009] (see Table 1 for Web links and references) and from the European Space Agency's GlobColour project. For this analysis, we used remotely sensed level 3 (i.e., binned and mapped) monthly and daily *Chl-a* data sets that were derived using standard case 1 water algorithms [*O'Reilly et al.*, 1998; *Morel and Maritorena*, 2001]. Any single ocean color sensor has a limited daily coverage resulting from gaps between the swaths, Sun glint, and cloud cover. Merging data from multiple sensors, if data from more than one sensor are available, will increase the coverage due to the combination of patchy and uneven daily coverage from sensors viewing

[1]Scripps Institution of Oceanography, University of California San Diego, La Jolla, California, USA.
[2]University of Maryland, College Park, Maryland, USA.
[3]Institute for Marine and Antarctic Studies, University of Tasmania, Hobart, Tasmania, Australia.
[4]Facultad de Ciencias del Mar, Universidad Autónoma de Sinaloa, Mazatlán, Sinaloa, México.

0148-0227/10/2010JC006500

Table 1. Data Sources Used in This Investigation

Variable	Description	Source and Reference
Chl-a	Level 3 monthly and daily gridded values from OCTS and SeaWiFS	http://oceancolor.gsfc.nasa.gov [*McClain*, 2009]
Chl-a	GlobColour, merged from multiple sensors	http://www.globcolour.info http://www.globcolour.info /CDR_Docs/GlobCOLOUR_PUG.pdf
Sea surface temperature	AVHRR Pathfinder version 5	http://www.nodc.noaa.gov/SatelliteData/pathfinder4km/ [*Kilpatrick et al.*, 2001]
Surface winds	Cross-calibrated Multi-Platform (SSM/I, TMI, AMSR-E, SeaWinds on QuikSCAT and ADEOS-II)	http://podaac.jpl.nasa.gov/DATA_CATALOG/ccmpinfo. html [*Ardizzone et al.*, 2009; *Atlas et al.*, 2008, 2009]
Mixed-layer climatology	Monthly means from hydrography	http://www.locean-ipsl.upmc.fr/~cdblod/mld.html [*de Boyer Montégut et al.*, 2004]
	From a global model	http://www.science.oregonstate.edu/ocean.productivity/ inputMldData.htm [*Behrenfeld et al.*, 2005]

the ocean at slightly different times and geometries. Compared to data from individual sensors, the merged products from three sensors (SeaWiFS, MERIS, and MODIS-Aqua) have approximately twice the mean global coverage and lower uncertainties in the retrieved variables [*Maritorena et al.*, 2010]. We therefore used *Chl-a* data merged by GlobColour from multiple sensors (combining SeaWiFS, MERIS, and MODIS-Aqua) with weighted averaging whenever possible (April 2002 to October 2009) and data from individual sensors (OCTS, November 1996 to June 1997; SeaWiFS, September 1997 through March 2002) during periods when only the single sensor data were available. While small but systematic differences exist between the products of individual sensors, the large-scale *Chl-a* distributions produced by the major ocean color missions are consistent over a wide range of conditions [*Morel et al.*, 2007; *Djavidnia et al.*, 2010]. We expect that the merged product based on standard case 1 water algorithms should have better coverage, higher quality, and lower uncertainty than the data from individual sensors, similar to when using the semianalytical model-based data merger [*Maritorena et al.*, 2010]. The latest versions of the data available at the time were used (e.g., reprocessing 2009.0 for SeaWiFS data, reprocessing 2007 for the merged data and the other sensors). Daily *Chl-a* data sets were composited into 5 day (pentad) time series from November 1996 to October 2009.

[4] Anomalies for both monthly and 5 day *Chl-a* time series were created by first by calculating the average value for each pixel and each month or pentad and then by using the ratio of the value during the current period (month or pentad) to the mean value of the respective time period (month or pentad). In other words, *Chl-a* is normalized by either monthly or pentad climatological value. The ratio anomaly was expressed as percentage anomaly, i.e., $100 \times (\text{Anomaly} - 1)$. The logarithm of the ratio anomaly is equivalent to the commonly used anomaly of log(*Chl-a*) minus the long-term seasonal mean of log(*Chl-a*). Monthly *Chl-a* data were used in most of the analysis performed here. The 5 day *Chl-a* anomalies were used only in the cross-spectrum analysis.

[5] Monthly sea surface temperature (SST) data were obtained from the AVHRR Pathfinder version 5 data set, an update of the NOAA/NASA Pathfinder data described by *Kilpatrick et al.* [2001]. SST monthly anomalies were created by subtracting the monthly mean value from the current monthly value. The high heat capacity of the ocean produces intrinsically slower variations in SSTs in most of the open ocean compared to the rapid responses and patchiness of *Chl-a*. Thus, we considered both pentad and monthly anomalies for *Chl-a* but only monthly anomalies for SSTs. For the large-, basin-scale variability we are interested in here, monthly anomalies proved appropriate for all variables.

[6] For wind fields, we used cross-calibrated multiplatform (CCMP) ocean surface winds [*Ardizzone et al.*, 2009; *Atlas et al.*, 2008, 2009] derived through cross calibration and assimilation of data from SSM/I, TMI, AMSR-E, SeaWinds on QuikSCAT, and SeaWinds on ADEOS-II. These data sets are combined with conventional observations and with a starting estimate of the wind field using a variational analysis method. Level 3.5 pentad and monthly wind data have 25 km spatial resolution. For this study, we used wind speed (U, m/s) provided as part of the CCMP data set, wind speed square (which is roughly proportional to wind stress under the assumption of a constant drag coefficient), and wind speed cubed (which is proportional to wind stress given a drag coefficient that depends on wind speed) [*Hellerman and Rosenstein*, 1983; *Yelland et al.*, 1998]. We also consider the zonal and meridional components of wind speed (u and v, m/s) and pseudostress (uU and vU, m^2/s^2). Monthly and pentad anomalies of the wind variables were constructed by subtracting the long-term mean value of the respective period from the value during each individual period. The CCMP wind data were available from July 1987 to December 2008 and the overlapping period during which both *Chl-a* wind data were available extended from November 1996 to December 2008. As a proxy for upwelling and the associated nutrient flux along the equator, we calculated the meridional wind divergence as the north-south gradient in v (m/s/km).

[7] For climatological ocean mixed-layer depth, we used monthly climatological fields computed by *de Boyer Montégut et al.* [2004] from hydrographic data. Interannual variability in the mixed-layer depth was obtained from model results [*Behrenfeld et al.*, 2005]. The model mixed-layer depths perform well in the tropics, and hence we only use them in the tropics and not in the extra-tropics, where validation data are comparatively sparse. Monthly MLD anomalies were created by subtracting the monthly mean value from the current monthly value.

3. Wind Speed and Chlorophyll Correlations

[8] *Chl-a*, a measure of phytoplankton biomass and biological productivity, is expected to depend on the avail-

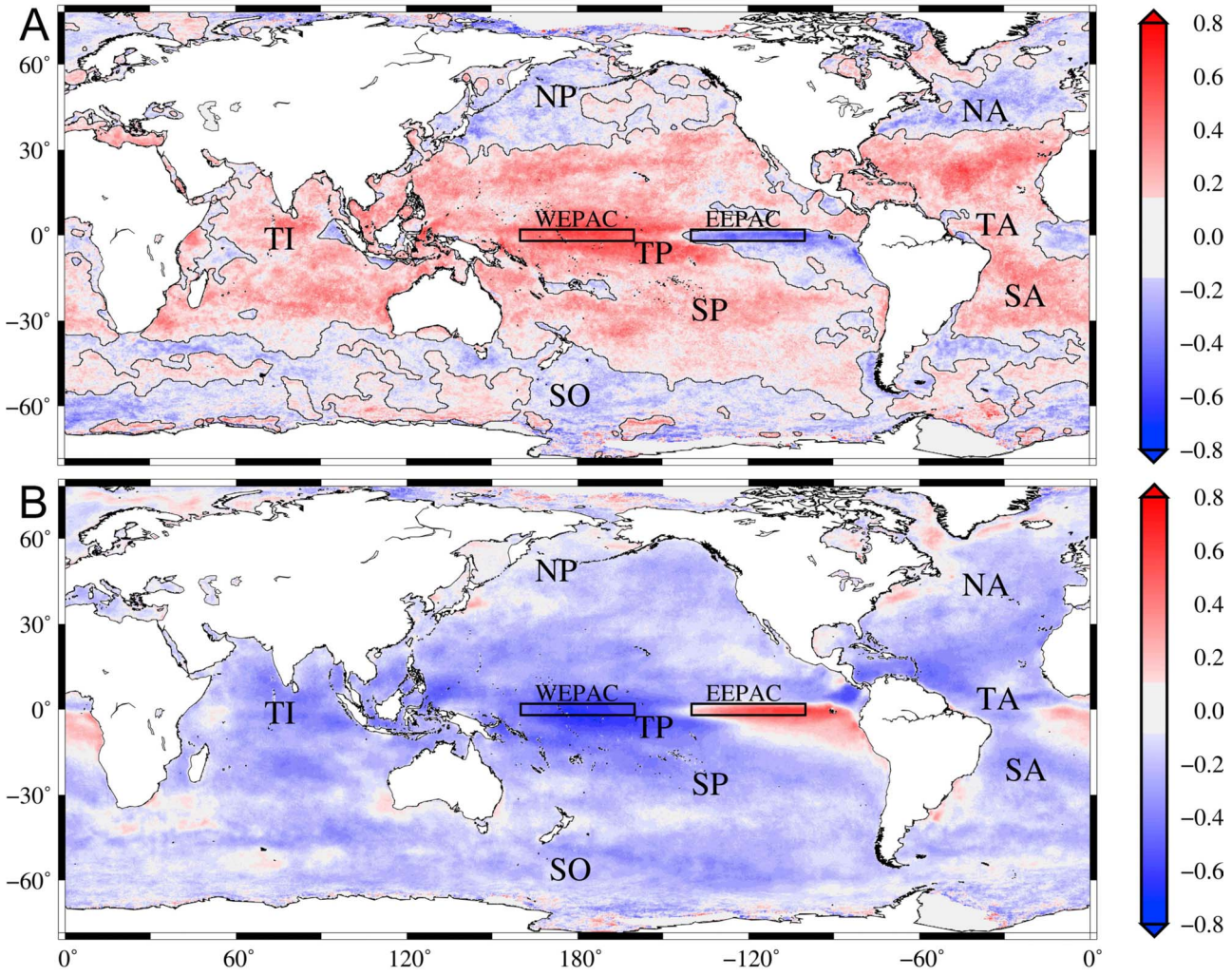

Figure 1. (a) Correlation coefficient (R) between monthly anomalies of wind speed and *Chl-a*. $N = 144$ (corresponding to the number of months of data available), the critical value, R_{crit} ($P < 0.05$) = 0.164, R_{crit} ($P < 0.01$) = 0.214, i.e., the correlation in the red and blue areas is statistically significant ($P < 0.05$). The selected areas in Western Equatorial Pacific (WEPAC, 2°N–2°S, 160°E–160°W) and Eastern Equatorial Pacific (EEPAC, 2°N–2°S, 140°W–100°W) along the equator are shown. The black curves are contour lines of $R = 0$. TI, Tropical Indian Ocean; NP, North Pacific; TP, Tropical Pacific; SO, Southern Ocean; SP, South Pacific; NA, North Atlantic; TA, Tropical Atlantic; SA, South Atlantic. (b) Correlation coefficient between monthly wind speed and sea surface temperature anomalies, $N = 258$, the critical value, R_{crit} ($P < 0.05$) = 0.122, R_{crit} ($P < 0.01$) = 0.160. The correlation in the red and blue areas is statistically significant ($P < 0.05$).

ability of light and nutrients. Light levels are high at the ocean surface, so phytoplankton will experience strong light and potentially rapid growth if they are confined to the top of the ocean and unable to mix down to deeper levels. Nutrient levels tend to be high in the deep ocean, and processes that allow deep water to mix into the surface euphotic zone will supply nutrients to support biological growth (although nutrients can also have atmospheric or continental origins).

[9] Wind is one factor governing upwelling and vertical mixing into the upper ocean, and wind also influences the depth of the ocean's surface mixed layer. In Figure 1a we show the correlation between monthly anomalies of wind speed and *Chl-a*. Figure 1 shows statistically significant patterns over the world ocean with positive correlations in the tropics and subtropical gyres and negative correlations in the subpolar gyres, the eastern tropical Pacific, and the eastern tropical Atlantic. Correlations that are not statistically significant at the 95% level are shaded gray in Figure 1. While the correlations are not large enough to explain all *Chl-a* variability, the large-scale patterns in Figure 1a imply that wind speed fluctuations have a measurable influence on *Chl-a*. It is essential that the correlations be calculated between the *Chl-a* values normalized by monthly climatological means and the wind anomalies, as discussed in section 2. Otherwise the annual cycle would dominate the correlations (e.g., at midlatitudes, the typically strong winds and low *Chl-a* in the winter would produce a strong negative correlation).

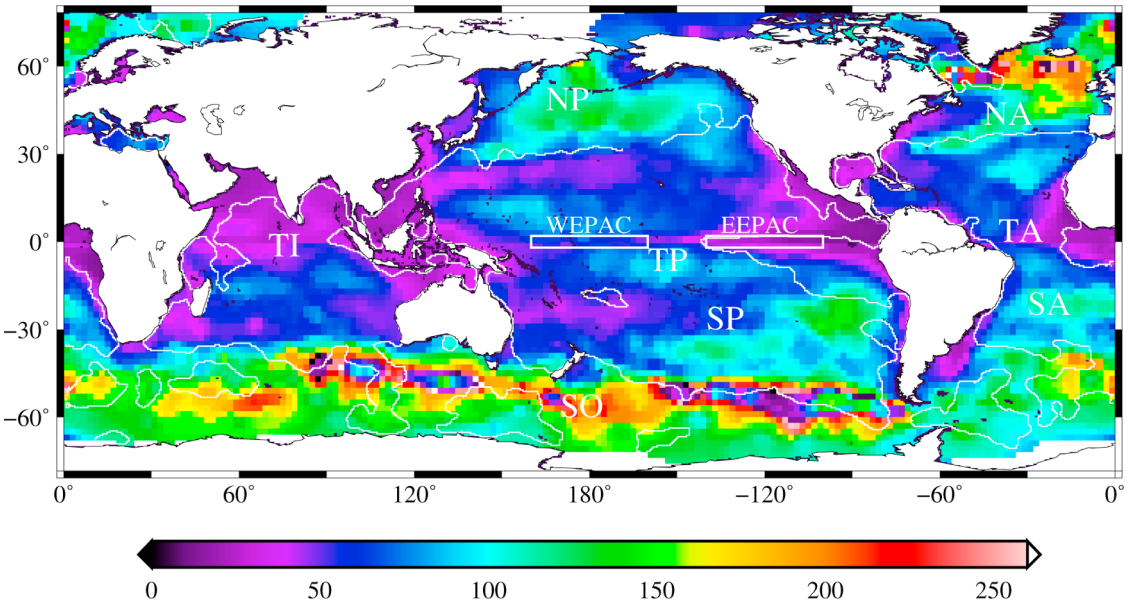

Figure 2. The upper mixed layer depth in spring (March in the Northern Hemisphere and September in the Southern Hemisphere) with the simplified contours separating regions with positive correlations between *Chl-a* and wind speed anomalies from those with negative correlations (as in Figure 1a). The monthly mixed layer depth climatology is based on the 0.2°C threshold criterion [*de Boyer Montégut et al.*, 2004].

[10] Formally, the strength of wind-induced upwelling and mixing is governed by wind stress rather than wind speed. We therefore also calculated the correlations between monthly anomalies of *Chl-a* and anomalies of squared or cubed wind speed (not shown), both of which produced correlation patterns that were essentially identical to those shown in Figure 1a.

[11] The large-scale correlation patterns between wind speed and *Chl-a* suggest different limiting factors for phytoplankton biomass in different parts of the world ocean. Positive correlations that occur through much of the tropics and subtropics are consistent with the idea that phytoplankton growth and biomass are primarily limited by the upward flux of nutrients and that stronger winds can increase this flux by increasing vertical mixing, likely by deepening the mixed layer. The idea that stronger winds deepen the mixed layer is supported by Figure 1b, which shows that the correlation between monthly anomalies of wind speed and SST is negative over most of the world ocean. This pattern is consistent with the hypothesis that in most regions increased wind speed cools the surface by vertical mixing (by breaking down the stratification built by solar flux, inducing upwelling of colder subsurface waters) and by increasing evaporation. Areas with positive correlation between monthly wind speed anomalies and SST anomalies, e.g., in the eastern tropical Pacific and eastern tropical Atlantic, are dominated by the interannual modes of variability [*Murtugudde et al.*, 1999; *Signorini et al.*, 1999] and will be discussed in section 4.

[12] In contrast to the mostly tropical and subtropical regions with positive correlations between wind speed and *Chl-a*, the subpolar gyres of the North Pacific, North Atlantic, and Southern Ocean have an opposite response, with strong winds corresponding to reduced *Chl-a* concentrations, and this points to a different process compared with wind speed/SST interactions. The negative correlation between wind and *Chl-a* can be explained if strong winds tend to increase the depth of vertical mixing sufficiently to remove phytoplankton from the euphotic zone and therefore reduce their average light levels. Indeed, these regions of negative correlation correspond well to regions with deep late winter/early spring mixed layers, as shown in Figure 2. By the same token, deeper mixed layers and colder temperatures render winds less effective in cooling SSTs, resulting in weak correlations between the two [*Seager and Murtugudde*, 1997].

[13] Early spring mixed layers are plotted in Figure 2, because they are typically the deepest mixed layers observed during the year. The mixed layer becomes shallower during the summer, and water that was contained within the mixed layer in spring is below the base of the mixed layer in summer. Regions with deep spring mixed layers may have shallow summer or fall mixed layers, but the water just below these shallow mixed layers will typically have low stratification. Therefore, small anomalous increases in summer wind can easily remix the upper ocean and reestablish deep mixed layers, which would tend to decrease *Chl-a*, relative to the seasonal average. Both in the North Pacific and North Atlantic the correlations between *Chl-a* and wind speed anomalies change from negative to positive where the spring mixed layer becomes shallower than about 70 m along a generally equatorward gradient. Also, in comparison with the North Pacific, the North Atlantic has deeper mixed layers and more negative correlation between *Chl-a* and wind speed anomalies. In the Southern Ocean, spring mixed layers are particularly deep in the regions of intermediate or mode water formation along the northern flank of the Antarctic Circumpolar Current in the Indian and Pacific sectors. Within these regions, *Chl-a* is negatively correlated with

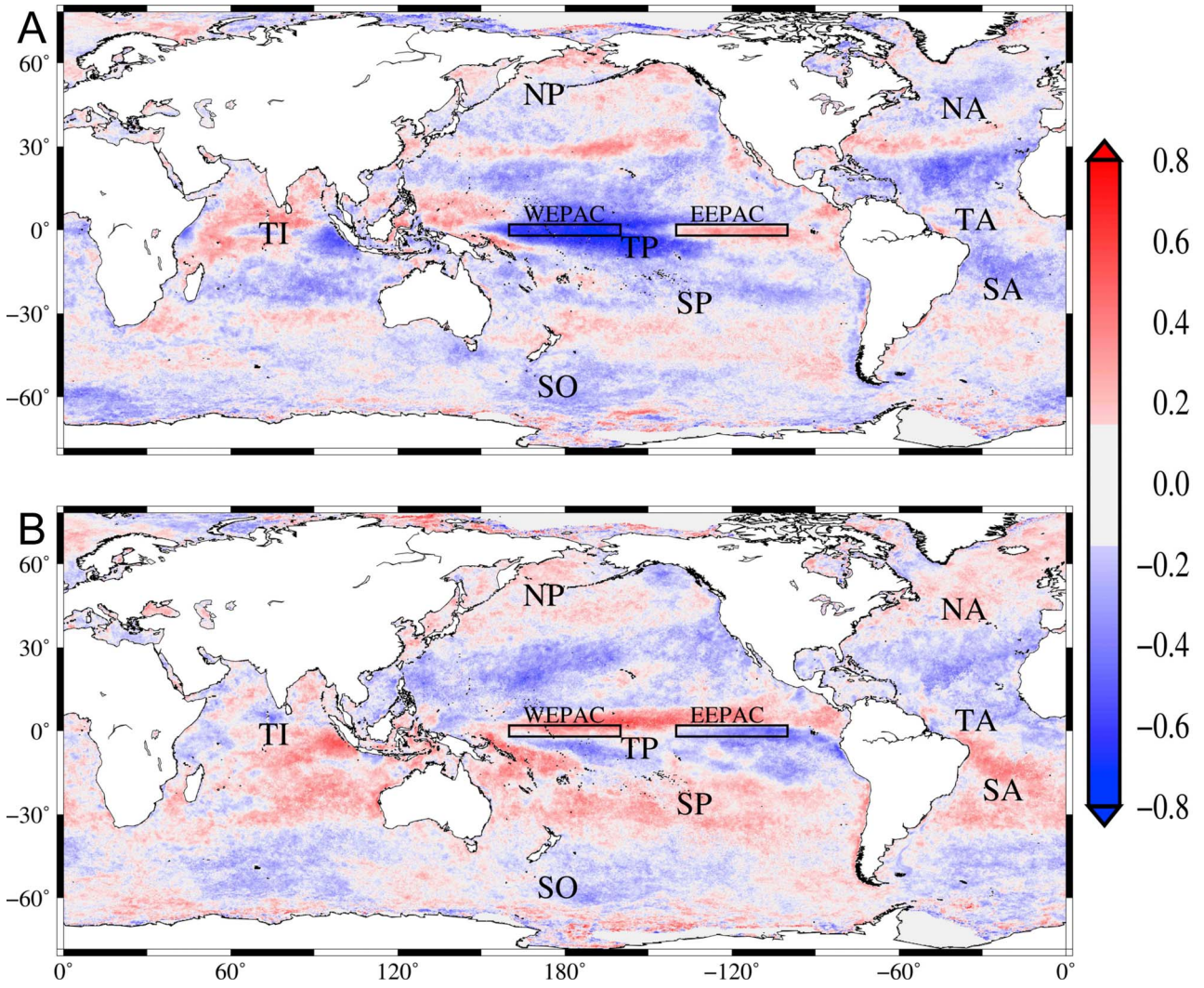

Figure 3. Correlations between monthly anomalies of *Chl-a* and anomalies of (a) the eastward wind pseudostress (*uU*, m^2/s^2) and (b) the northward wind pseudostress (*vU*, m^2/s^2).

wind speed, whereas to the north, where mixed layers are shallower, *Chl-a* is positively correlated with wind speed. A number of patches with positive wind speed/*Chl-a* correlations occur inside the Southern Ocean, e.g., the Scotia Sea, northeast from the Antarctic Peninsula, and these regions tend to have shallower spring mixed layers.

[14] Within these two general scenarios, we acknowledge that the factors limiting phytoplankton growth can change during the annual cycle, particularly in temperate and polar environments. In addition, at high latitudes the light levels during winter are not sufficient to derive *Chl-a* from water-leaving radiances, and therefore the correlation patterns at high latitudes are naturally weighted toward the phytoplankton growth period. The correlation patterns are typically spatially variable or not significant in these regions (the Arctic and high-latitude Southern Ocean), where the growing season covers both deeply mixed and stratified periods, and near-surface stratification is often controlled by the effects of salinity (e.g., through melting of ice).

[15] Figure 3 shows the corresponding correlation patterns between monthly anomalies of *Chl-a* and the anomalies of eastward (*uU*) or northward (*vU*) wind pseudostress. Some areas, e.g., eastern North Atlantic (20°N–30°N) off Africa, have a relatively deep mixed layer (~100 m) in the spring but still show positive correlation between wind speed anomalies and *Chl-a* anomalies (Figure 1a). It is likely that the fertilizing effect of the Saharan dust associated with strong winds drives the positive correlation in the subtropical North Atlantic. This supposition is supported by the observed negative correlation with the eastward wind pseudostress anomaly (Figure 3a), i.e., positive correlation with the stronger than usual westward winds that bring the Saharan dust over the Atlantic. Atmospheric dust deposition may also affect some other areas such as the Arabian Sea, the South China Sea, and the Patagonian shelf.

[16] As demonstrated by Figures 1 and 3, the correlation patterns between monthly anomalies of *Chl-a* or SST on the one hand and monthly anomalies of wind speed or wind components on the other show different patterns, each conveying a certain relationship. These correlation patterns as well as the correlation patterns between monthly *Chl-a* anomaly and the nonnormalized (i.e., without taking the

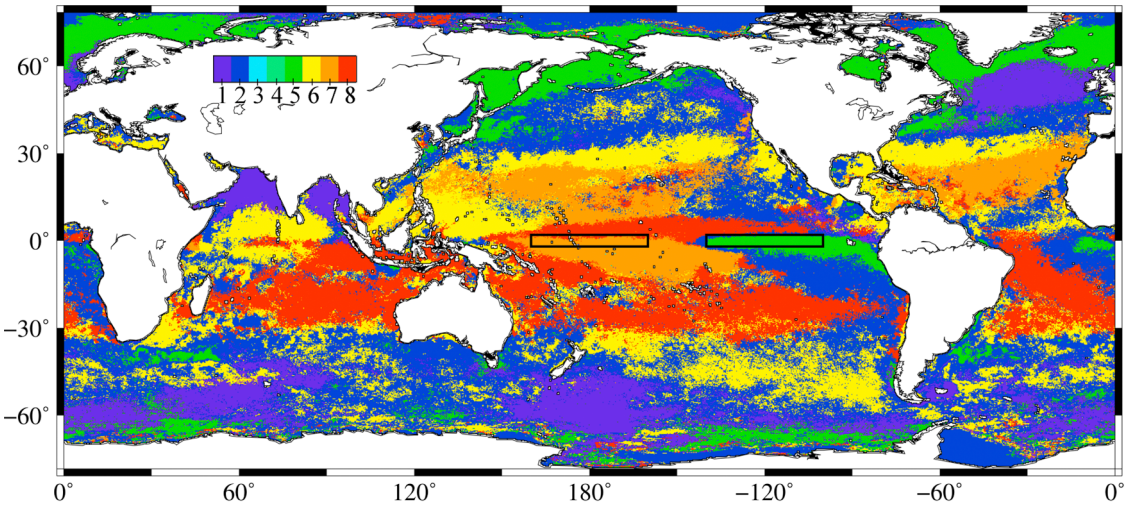

Figure 4. Results of the *k* means cluster analysis using the correlation coefficients between the following seven pairs of variables: (1) monthly *Chl-a* anomaly and eastward wind pseudostress anomaly, (2) monthly *Chl-a* anomaly and northward wind pseudostress anomaly, (3) monthly *Chl-a* anomaly and wind speed anomaly, (4) monthly *Chl-a* anomaly and eastward wind pseudostress, (5) monthly *Chl-a* anomaly and northward wind pseudostress, (6) monthly *Chl-a* anomaly and wind speed, and (7) monthly SST anomaly and wind speed anomaly.

anomaly) wind speed and wind components were used in the *k* means cluster analysis [*Hartigan and Wong*, 1979] to find regions with similar correlative relationships. The *k* means clustering method assigns data points into *k* groups such that the sum of squares from points to the computed cluster centers is minimized. As input we used the correlation coefficients between the following seven pairs of variables: (1) monthly *Chl-a* anomaly and eastward wind pseudostress anomaly, (2) monthly *Chl-a* anomaly and northward wind pseudostress anomaly, (3) monthly *Chl-a* anomaly and wind speed anomaly, (4) monthly *Chl-a* anomaly and eastward wind pseudostress, (5) monthly *Chl-a* anomaly and northward wind pseudostress, (6) monthly *Chl-a* anomaly and wind speed, and (7) monthly SST anomaly and wind speed anomaly. It is important to note that the seven-dimensional input vector of correlation coefficients had no explicit information on the position of each point. The resulting clusters of similar correlations (Figure 4) show coherent spatial patterns and share common features with previous analysis [e.g., *Longhurst et al.*, 1995] but are based solely on the correlations with wind. The mostly spatially coherent patterns in the output suggest that the analysis has skill at identifying regions with common statistical characteristics. With this kind of analysis, a number of geographically distant clusters of pixels exhibit similar correlations and therefore receive the same cluster number. For example, the cluster shown with green pixels in Figure 4 is found not only at high northern and southern latitudes but also in eastern tropical Pacific and Atlantic. In a biogeographic domain analysis these should be counted as separate domains. While we assume only two limiting factors (light and nutrients), the combination of spatial variations in the correlations between the wind components on the one hand and *Chl-a* or SST on the other results in many spatially coherent regions with a particular set of positive or negative influences. The total number of clusters is not fixed in the *k* means cluster analysis and a number of methods exist to find the optimal number of clusters. Here we subjectively chose eight clusters as that resulted in patterns that looked reasonable based on previous literature on this subject. Further analysis is needed to find the optimum number of clusters that best correspond to the biogeographic domains as understood in biological oceanography.

4. Equatorial Upwelling Patterns

[17] The most complex features including the highest correlations between *Chl-a* and winds can be seen in the equatorial regions. Here the western Pacific (WEPAC), with the highest positive correlation between *Chl-a* and wind speed is adjacent to the eastern Pacific (EEPAC) with the highest negative correlation between *Chl-a* and wind speed. We selected areas in the Western Equatorial Pacific (WEPAC, 2°N–2°S, 160°E–160°W) and Eastern Equatorial Pacific (EEPAC, 2°N–2°S, 140°W–100°W) to show the relationships in more detail.

[18] The most striking correlation between wind speed and *Chl-a* anomalies is evident in the western tropical Pacific (Figure 5), where there is almost a linear correlation between the anomalies of these two variables, except during the 1998 ENSO that produced exceptionally strong phytoplankton blooms along the equator near 170°E during the transition between El Niño and La Niña in March–June 1998 [*Murtugudde et al.*, 1999; *Ryan et al.*, 2002]. The 1998 La Niña event stands out in Figure 5 as having anomalously high *Chl-a* even relative to the anomalously high wind speeds. The correlation with wind speed is primarily driven by the negative linear correlation between *Chl-a* and the zonal wind velocity (negative *u*, characteristic of upwelling-favorable winds, correlated with positive *Chl-a*), which occurs both north and south of the equator (Figures 6a and 6c). (Note that in Figure 6 we show zonal and meridional

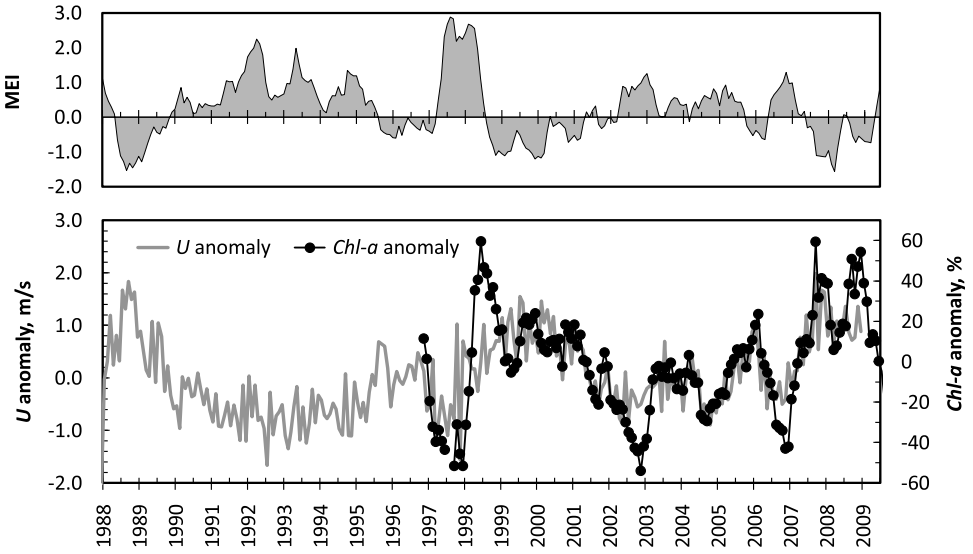

Figure 5. Time series of monthly anomalies of (left axis) wind speed (U, m/s) and (right axis) *Chl-a* (%) in the northern WEPAC box (2°N–0°N, 160°E–160°W). $R = 0.705$, $P < 0.01$. The Multivariate ENSO index (MEI, http://www.esrl.noaa.gov/psd/data/climateindices/list/) is shown for comparison.

wind components rather than anomalies in order to indicate clearly the direction of the wind.)

[19] The mechanisms invoked to explain the particular blooms have included the island effect of the Kiribati islands [*Messié et al.*, 2006], the erosion of the barrier layer in the western Pacific warm pool [*Murtugudde et al.*, 1999], and changes in the dynamics of the New Guinea coastal currents that feed the equatorial undercurrent [*Ryan et al.*, 2006]. The 1997–1998 El Niño/Southern Oscillation (ENSO) event was comparatively warm, but since mid-1998, the equatorial

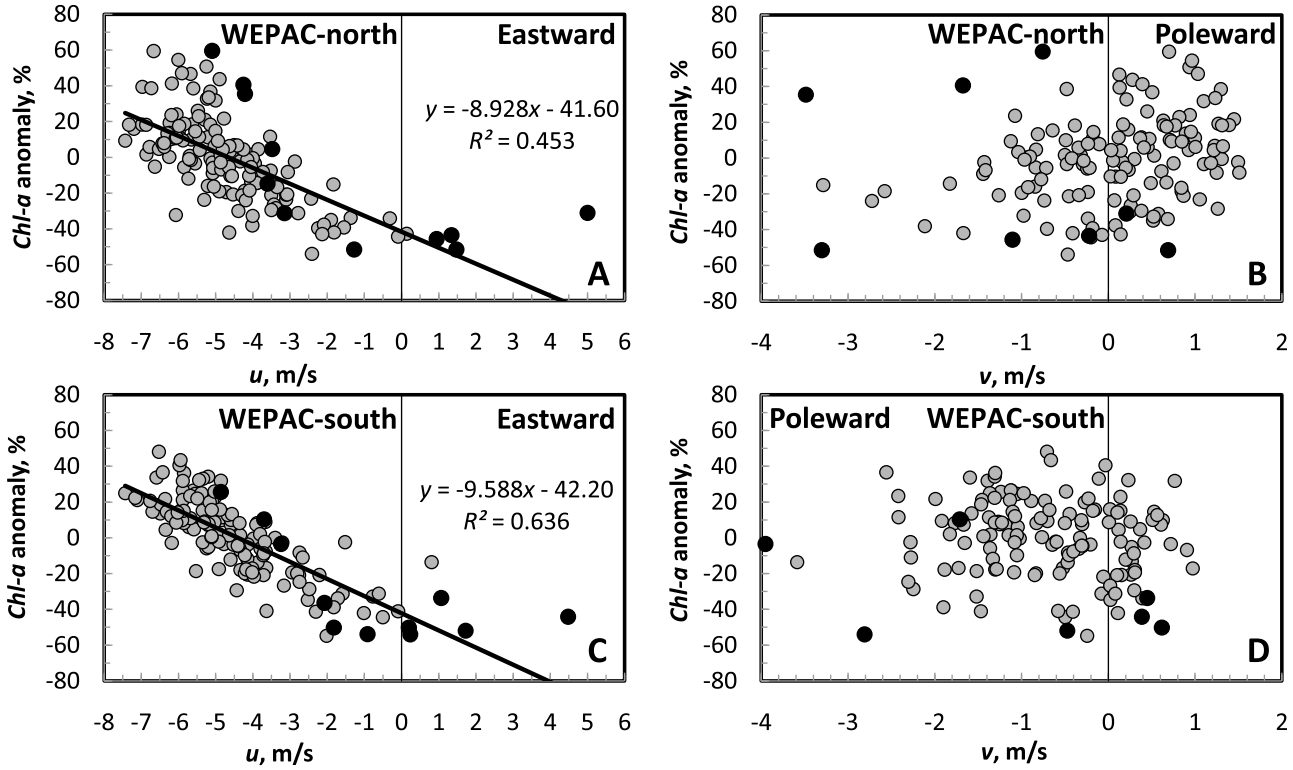

Figure 6. Scatter plots of the monthly *Chl-a* anomaly versus (a and c) eastward wind velocity (u) and (b and d) northward wind velocity (v) in the WEPAC area (a and b) north of the equator and (c and d) south of the equator. The correlations are slightly stronger if anomalies are used instead of the wind velocities themselves, but for simplicity we use the wind velocities here. The black circles are the months during the strong El Niño event of June 1997 to June 1998.

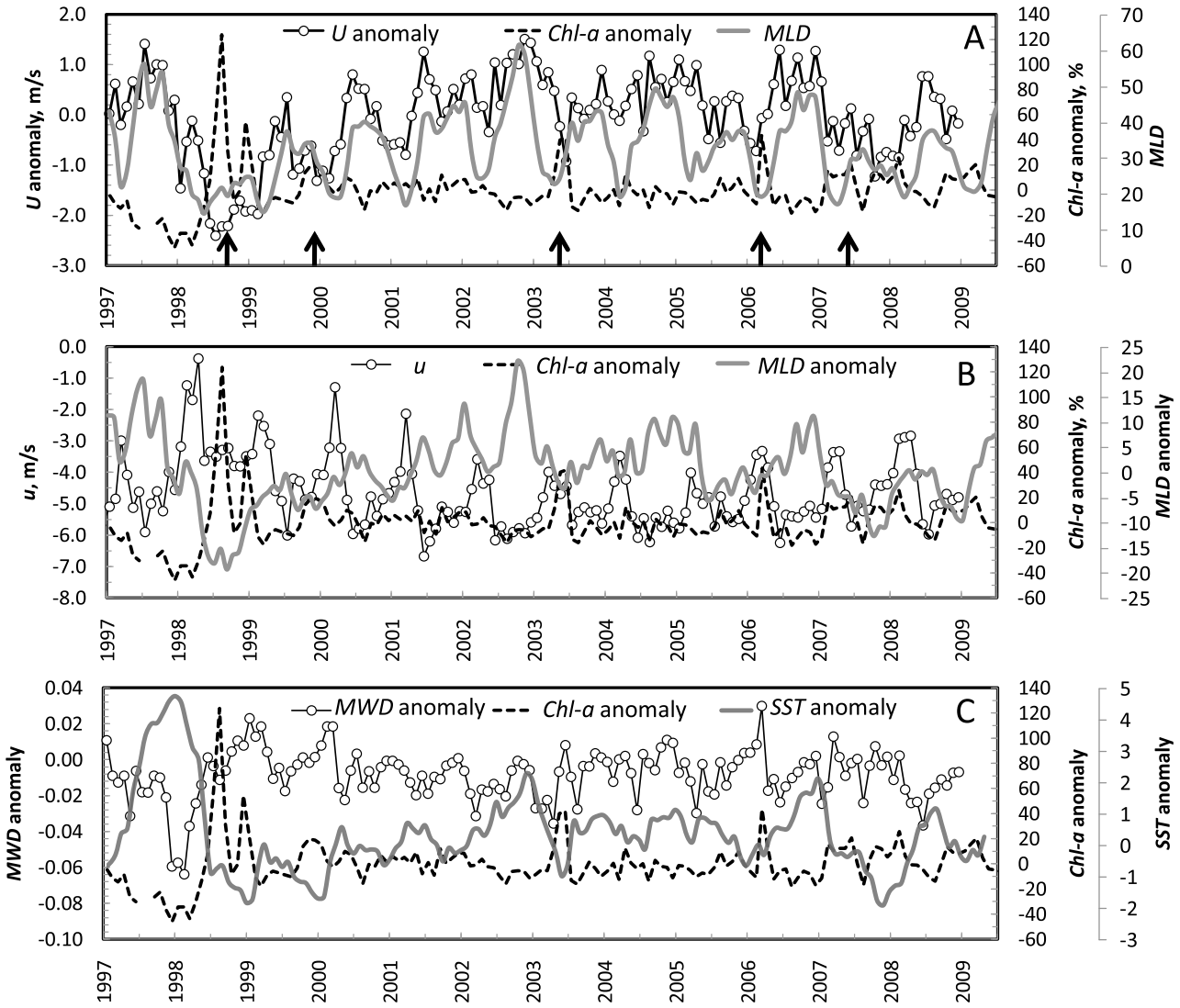

Figure 7. Monthly mean time series in the southern EEPAC box. (a) Wind speed (*U*) anomaly, mixed layer depth (MLD) and *Chl-a* anomaly. *Chl-a* bloom events (↑) occurred at dips in *U* anomaly in 1998, 1999/2000, 2003, 2006, and 2007. (b) Eastward wind velocity (*u*), MLD anomaly, and *Chl-a* anomaly. (c) Meridional wind divergence (MWD), SST, and *Chl-a* anomalies. Significant correlations: *R* (*U* anomaly, *Chl-a* anomaly) = −0.438; *R* (MLD, *Chl-a* anomaly) = −0.370; *R* (MLD anomaly, *Chl-a* anomaly) = −0.516; *R* (MWD anomaly, *Chl-a* anomaly) = 0.371; *R* (SST anomaly, *Chl-a* anomaly) = −0.671; R_{crit} = 0.214 ($P < 0.01$); N = 144.

Pacific has experienced only weak El Niño events in 2002–2003, 2004–2005, and 2006–2007.

[20] The meridional winds are relatively weak (±2 m/s) in the WEPAC area and show no correlation with *Chl-a* (Figures 6b and 6d). The direction of the north-south wind component is variable but more often poleward both north and south of the equator (positive *v* in the north and negative *v* in the south). Since the monsoonal regime intrudes into the western Pacific warm pool region, the meridional component is expected to be noisier than the zonal winds. The decaying stages of the strong ENSO event during the spring of 1998 resulted in the strongest southward winds both north and south of the equator driven by the deep convection that had shifted to the central-equatorial Pacific [*Murtugudde et al.*, 2004].

[21] In the EEPAC the correlations between wind speed and *Chl-a* are opposite to those in the WEPAC area: *Chl-a* anomaly is inversely related to wind speed anomaly (Figure 1), positively correlated to eastward wind stress anomaly and negatively correlated to northward wind stress anomaly (Figure 3). However, the correlations are weaker than in the WEPAC and the relationships are not linear (Figure 7). The EEPAC is a region dominated by mixed layer-thermocline interactions and nutrient entrainment processes that drive enhanced production, although iron limitation produces high nutrient-low chlorophyll (HNLC) conditions [*Coale et al.*, 1996]. Prevailing winds are westward on the equator but weaken each year during boreal winter or spring as well as during El Niño events (see Figure 7b, which shows the zonal wind rather than its anomaly). At these times westerly wind

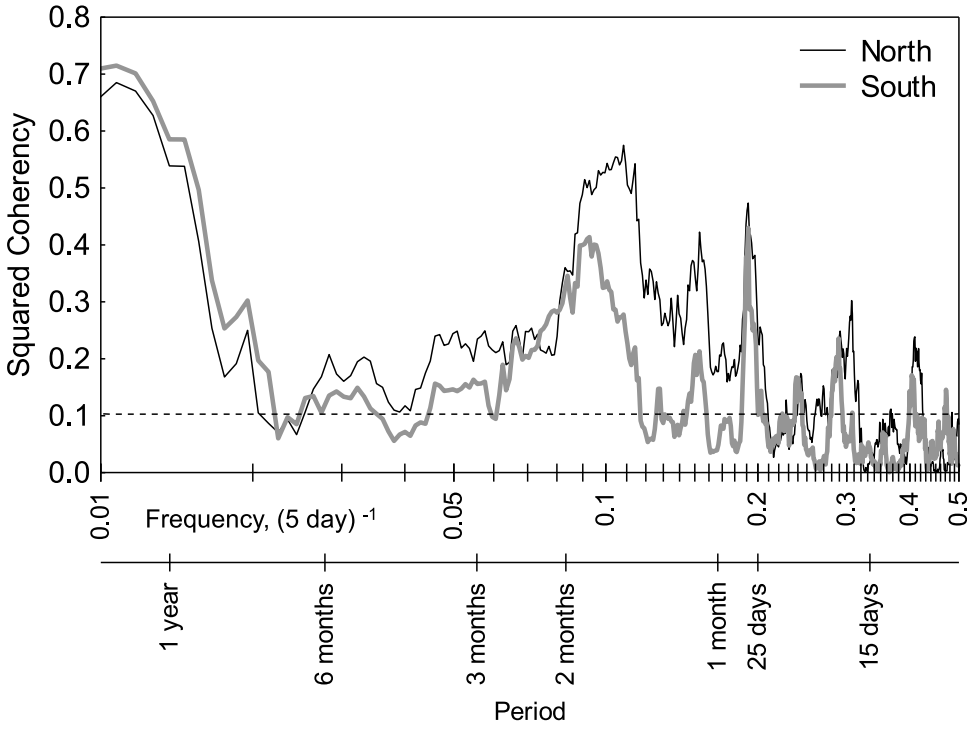

Figure 8. Cross-spectral square coherency functions between time series of 5 day anomalies of wind speed and 5 day anomalies of *Chl-a* in the northern (2°N–0°N, 160°E–160°W) and southern (0°S–2°S, 160°E–160°W) WEPAC area. The horizontal short dashes indicate the 95% critical value for testing the null hypothesis of zero coherence [*von Storch and Zwiers*, 1999].

bursts in the western Pacific warm pool region generate equatorial Kelvin waves that propagate eastward along the equator, resulting in warm SSTs in the EEPAC region, a depressed thermocline, and deep mixed layers, which can reduce biological productivity [*Aufdenkampe et al.*, 2002; *Chavez et al.*, 1998]. *Ryan et al.* [2006] attributed blooms in 1998, 2003, and 2005 to shoaling of the equatorial Pacific thermocline and enhanced iron in the New Guinea coastal undercurrent, which feeds into the equatorial undercurrent. Similarly, Figures 7a–7c indicate anomalous *Chl-a* blooms in 1998, 1999/2000, 2003, 2006, and 2007 that occur in boreal late winter or spring when westward winds remain weak longer than usual, so that wind speeds are anomalously low for the season (Figures 7a and 7b). These anomalously low winds produce the negative correlation between anomalies of wind speed and *Chl-a* (Figure 1a), but the wind components u and v are not at their extremes during these events. At the times of these *Chl-a* blooms, meridional wind stress divergence (Figure 7c) is anomalously high, which is consistent with enhanced upwelling which favors production of cool SST anomalies (Figure 7c) and shallow mixed layer anomalies (Figure 7b). The 1998 and 1999 *Chl-a* blooms differ in timing and strength from the later blooms but correspond to similar patterns of low wind speed, high wind stress divergence, and low SST. The exceptionally high 1998 peak in *Chl-a* occurred during the transition from El Niño and La Niña with moderate u toward the west (-3 m s^{-1}, Figure 7b) and weak v toward the north (1.5 m s^{-1}, data not shown) [*Murtugudde et al.*, 1999, 2004; *Ryan et al.*, 2002].

[22] Some of the overall correlations in Figures 1 and 3 might be caused by a single strong event (such as the 1997–1998 ENSO), but as shown by the above analysis, in most cases the correlation is spread over multiple time scales and involves multiple events (Figures 5–7). Cross-spectral analysis between time series of 5 day anomalies of wind speed and 5 day anomalies of *Chl-a* in the WEPAC area (Figure 4) confirms that significant coherence between wind speed and *Chl-a* exists over a range of periods from days to years. The broad peak between 1 and 3 months is likely related to the Madden Julian Oscillation [*Wheeler and Hendon*, 2004; *Waliser et al.*, 2005].

[23] In the tropical Indian Ocean there is no significant equatorial upwelling and the seasonal *Chl-a* signal is associated with the recirculation in the western equatorial region and the southeastern coast along Java and Sumatra [*Murtugudde et al.*, 1999]. The interannual variability associated with the Indian Ocean Dipole/Zonal Mode produces a boreal fall anomaly in *Chl-a* [*Murtugudde et al.*, 1999] and is seen as a small region of negative correlation in the far east in Figure 1. In the tropical Pacific and tropical Atlantic phytoplankton blooms are limited by the upward flux of nutrients through the thermocline as shown by the positive effect of higher wind speed in the central-western equatorial regions. Advection of nutrients from the eastern upwelling regions will add to this correlation. This pattern contrasts markedly with the mechanisms that appear to govern the North Pacific and especially the North Atlantic, where phytoplankton are limited by the average light level in the mixed layer, and the prevailing effect of winds is

negative as wind mixing tends to deepen the mixed layer beyond the euphotic zone depth. (Figure 8)

5. Summary and Conclusions

[24] This study has examined large-scale correlation patterns between winds and surface *Chl-a* concentrations. These patterns provide a consistent view of the main controlling factors of phytoplankton growth (nutrients or light). For most of the global ocean, high positive correlations occur in regions where the ocean mixed layer is comparatively shallow, and increased winds are readily able to deepen the mixed layer and entrain additional nutrients into the upper ocean. Strong negative correlations tend to occur in regions where late winter mixed layers are deep, and increased winds are likely to deepen the mixed layer enough to push phytoplankton out of the sunlit euphotic zone at the top of the ocean. Because of these distinctions between regions where increased winds appear to reduce light and regions where increased winds appear to increase nutrient availability, regions of strong positive and negative correlation map out distinct biogeochemical regimes within the world's oceans.

[25] Exceptions occur in the equatorial zone. Although the mixed layer is comparatively shallow along the equator, negative correlations nonetheless occur in the Eastern Equatorial Pacific and Eastern Equatorial Atlantic Oceans. These negative correlations are hypothesized to result from eastward propagating Kelvin wave dynamics that lead to a shoaling of the mixed layer in high wind speed conditions and therefore a remotely forced negative correlation between mixed-layer depth and wind speed.

[26] **Acknowledgments.** Financial support was provided by the NASA Ocean Biology and Biogeochemistry Program, the NASA Physical Oceanography Program, and the National Science Foundation. We thank the NASA Ocean Color Processing Group, PODAAC at JPL, and NOAA NODC for satellite data.

References

Ardizzone, J., R. Atlas, and R. N. Hoffman (2009), New multiplatform ocean surface wind product available, *Eos Trans. AGU*, *90*, 231.

Atlas, R., J. Ardizzone, and R. N. Hoffman (2008), Application of satellite surface wind data to ocean wind analysis, *Proc. SPIE*, 7087, doi:10.1117/12.795371.

Atlas, R., R. N. Hoffman, J. Ardizzone, S. M. Leidner, and J. C. Jusem (2009), Development of a new cross-calibrated, multiplatform (CCMP) ocean surface wind product, paper presented at AMS 13th Conference on Integrated Observing and Assimilation Systems for Atmosphere, Oceans, and Land Surface (IOAS-AOLS), Phoenix, Ariz.

Aufdenkampe, A. K., J. J. McCarthy, C. Navarette, M. Rodier, J. Dunne, and J. W. Murray (2002), Biogeochemical controls on new production in the tropical pacific, *Deep Sea Res., Part II*, *49*, 2619–2648.

Behrenfeld, M. J., E. Boss, D. A. Siegel, and D. M. Shea (2005), Carbon-based ocean productivity and phytoplankton physiology from space, *Global Biogeochem. Cycles*, *19*, GB1006, doi:10.1029/2004GB002299.

Chavez, F. P., P. G. Strutton, and M. J. McPhaden (1998), Biological-physical coupling in the central equatorial Pacific during the onset of the 1997–98 El Niño, *Geophys. Res. Lett.*, *25*(19), 3543–3546, doi:10.1029/98GL02729.

Chisholm, S. W., and F. M. M. Morel (1991), What controls phytoplankton production in nutrient-rich areas of the open sea?, *Limnol. Oceanogr.*, *36*, 1507–1970.

Coale, K. H., et al. (1996), A massive phytoplankton bloom induced by an ecosystem-scale iron fertilization experiment in the Equatorial Pacific Ocean, *Nature*, *383*, 495–501, doi:10.1038/383495a0.

de Boyer Montégut, C., G. Madec, A. S. Fischer, A. Lazar, and D. Iudicone (2004), Mixed layer depth over the global ocean: An examination of profile data and a profile-based climatology, *J. Geophys. Res.*, *109*, C12003, doi:10.1029/2004JC002378.

Denman, K. (1973), A time-dependent model of the upper ocean, *J. Phys. Oceanogr.*, *3*, 173–184.

Devred, E., S. Sathyendranath, and T. Platt (2007), Delineation of ecological provinces using ocean colour radiometry, *Mar. Ecol. Prog. Ser.*, *346*, 1–13, doi:103354/meps07149.

Djavidnia, S., F. Mélin, and N. Hoepffner (2010), Comparison of global ocean colour data records, *Ocean Sci.*, *6*, 61–76, doi:10.5194/os-6-61-2010.

Esaias, W., R. Iverson, and K. Turpie (2000), Ocean province classification using ocean colour data: Observing biological signatures of variations in physical dynamics, *Global Change Biol.*, *6*, 39–55.

Hartigan, J. A., and M. A. Wong (1979), Algorithm AS 136: A *k* means clustering algorithm, *Appl. Stat.*, *28*, 100–108.

Hellerman, S. and M. Rosenstein (1983), Normal monthly wind stress over the world ocean with error estimates, *J. Phys. Oceanogr.*, *13*, 1093–1104.

Kilpatrick, K. A., G. P. Podesta, and R. Evans (2001). Overview of the NOAA/NASA Advanced Very High Resolution Radiometer Pathfinder algorithm for sea surface temperature and associated matchup database, *J. Geophys. Res.*, *106*(C5), 9179–9197, doi:10.1029/1999JC000065.

Longhurst, A., S. Sathyendranath, T. Platt, and C. Caverhill (1995), An estimate of global primary production in the ocean from satellite radiometer data, *J. Plankton Res.*, *17*, 1245–1271.

Maritorena, S., O. H. F. d'Andon, A. Mangin, and D. A. Siegel (2010), Merged satellite ocean color data products using a bio-optical model: Characteristics, benefits and issues, *Remote Sens. Environ.*, *114*, 1791–1804, doi:10.1016/j.rse.2010.04.002.

McClain, C. R. (2009), A decade of satellite ocean color observations, *Annu. Rev. Mar. Sci.*, *1*, 19–42.

Messié, M., M.-H. Radenac, J. Lefévre, and P. Marchesiello (2006), Chlorophyll bloom in the western Pacific at the end of the 1997–1998 El Niño: The role of the Kiribati Islands, *Geophys. Res. Lett.*, *33*, L14601, doi:10.1029/2006GL026033.

Moore, T. S., J. W. Campbell, and M. D. Dowell (2009), A class-based approach to characterizing and mapping the uncertainty of the MODIS ocean chlorophyll product, *Remote Sens. Environ.*, *113*, 2424–2430.

Morel, A., Y. Huot, B. Gentili, P. J. Werdell, S. B. Hooker, and B. A. Franz (2007), Examining the consistency of products derived from various ocean color sensors in open ocean (case 1) waters in the perspective of a multisensor approach, *Remote Sens. Environ*, *111*, 69–88.

Morel, A., and S. Maritorena (2001), Bio-optical properties of oceanic waters: A reappraisal, *J. Geophys. Res.*, *106*(C4), 7763–7780, doi:10.1029/2000JC000319.

Murtugudde, R. G., S. R. Signorini, J. R. Christian, A. Busalacchi, C. R. McClain, and J. Picaut (1999), Ocean color variability of the tropical Indo-Pacific basin observed by SeaWiFS during 1997–1998, *J. Geophys. Res.*, *104*(C8), 18,351–18,366, doi:10.1029/1999JC900135.

Murtugudde, R. G., L. Wang, E. Hackert, J. Beauchamp, J. Christian, and A. Busalacchi (2004), Remote sensing of the Indo-Pacific region: Ocean colour, sea level, winds and sea surface temperatures, *Int. J. Remote Sens.*, *25*, 1423–1435.

Oliver, M. J., and A. J. Irwin (2008), Objective global ocean biogeographic provinces, *Geophys. Res. Lett.*, *35*, L15601, doi:10.1029/2008GL034238.

O'Reilly, J. E., S. Maritorena, B. G. Mitchell, D. A. Siegel, K. L. Carder, S. A. Garver, M. Kahru, and C. R. McClain (1998), Ocean color chlorophyll algorithms for SeaWiFS, *J. Geophys. Res.*, *103*(C11), 24,937–24,953, doi:10.1029/98JC02160.

Ryan, J. P., P. S. Polito, P. S. Strutton, and F. P. Chavez (2002), Unusual large-scale phytoplankton blooms in the equatorial Pacific, *Prog. Oceanogr.*, *55*, 263–285.

Ryan, J. P., I. Ueki, Y. Chao, H. Zhang, P. S. Polito, and F. P. Chavez (2006), Western Pacific modulation of large phytoplankton blooms in the central and eastern equatorial Pacific, *J. Geophys. Res.*, *111*, G02013, doi:10.1029/2005JG000084.

Platt, T. C., and S. Sathyendranath (1988), Oceanic primary production: Estimation by remote sensing at local and regional scales, *Science*, *241*, 1613–1620.

Sarmiento, J. L., and J. C. Orr (1991), Three-dimensional simulations of the impact of Southern Ocean nutrient depletion on atmospheric arbon dioxide and ocean chemistry, *Limnol. Oceanogr.*, *36*, 1928–1950.

Seager, R., and R. Murtugudde (1997), Ocean dynamics, thermocline adjustment, and regulation of tropical SST, *J. Clim.*, *10*, 521–534.

Siegel, D. A., S. C. Doney, and J. A. Yoder (2002), The North Atlantic spring phytoplankton bloom and Sverdrup's critical depth hypothesis, *Science*, *296*, 730–733.

Signorini, S. R., R. G. Murtugudde, C. R. McClain, J. R. Christian, J. Picaut, and A. J. Busalacchi (1999), Biological and physical signatures in

the tropical and subtropical Atlantic, *J. Geophys. Res.*, *104*(C8), 18,367–18,382, doi:10.1029/1999JC900134.

von Storch, H., and F. W. Zwiers (1999), *Statistical Analysis in Climate Research*, 484 pp., Cambridge Univ. Press, New York.

Waliser, D. E., R. Murtugudde, P. Strutton, and J.-L. Li (2005), Subseasonal organization of ocean chlorophyll: Prospects for prediction based on the Madden-Julian oscillation, *Geophys. Res. Lett.*, *32*, L23602, doi:10.1029/2005GL024300.

Wheeler, M., and H. Hendon (2004), An all-season real-time multivariate MJO index: Development of an index for monitoring and prediction, *Mon. Weather Rev.*, *132*, 1917–1932.

Yelland, M. J., B. I. Moat, P. K. Taylor, R. W. Pascal, J. Hutchings, and V. C. Cornell (1998), Wind stress measurements from the open ocean corrected for airflow distortion by the ship, *J. Phys. Oceanogr.*, *28*, 1511–1526.

S. T. Gille, M. Kahru, B. G. Mitchell, and H. Wang, Scripps Institution of Oceanography, University of California, San Diego, La Jolla, CA 92093-0218, USA. (mkahru@ucsd.edu)

M. Manzano-Sarabia, Facultad de Ciencias del Mar, Universidad Autónoma de Sinaloa, Mazatlán, Sinaloa, México.

R. Murtugudde, University of Maryland, 2207 CSS Bldg/ESSIC, College Park, MD 20742, USA.

P. G. Strutton, Institute for Marine and Antarctic Studies, University of Tasmania, Hobart, Tasmania, Australia.